PCCP

PAPER

View Article Online
View Journal

Cite this: DOI: 10.1039/d6cp01132b

Engineering halide composition to control structural and electronic properties in bismuth-based perovskite-inspired materials

Michael Zambrano-Angulo,[a] Adriana Pecoraro,[a] Roberto Grisorio,[b] Gian Paolo Suranna,[b] Michele Pavone[c] and Ana Belén Muñoz-García*[a]

Recent advances in photovoltaic technologies have established lead halide perovskites as benchmark materials for optoelectronic applications, but serious concerns persist regarding the toxicity of lead, their principal constituent element. In this context, bismuth-based perovskite-inspired materials have emerged as a promising lead-free alternative, offering comparable electronic characteristics. Here, we explore the structural, electronic and transport properties of **$Cs_3Bi_2I_9$** and **$Cs_3Bi_2Br_9$**, two perovskite-inspired materials with significant potential for photovoltaic and photocatalytic applications. With state-of-the-art first-principles calculations, we investigate the subtle effects of iodine/bromine (I/Br) mixing on the materials' physico–chemical properties. We predict a change in phase stabilities around 40% Br content: below 30% Br, the iodine-dominant $P6_3/mmc$ phase is stable, while beyond 40% Br, the bromine-dominant $P\text{-}3m1$ phase becomes energetically favorable, consistent with experimental observations. The electronic bandgap increases with Br content, and effective mass calculations indicate that electrons exhibit lower effective masses and higher mobility compared to holes, with hole localization intensifying as the Br content increases. Overall, our findings underscore the critical role of halogen composition in modulating the structural, electronic, and transport properties of these materials, providing valuable insights for optimizing halide contents in perovskite-inspired systems for next-generation optoelectronic applications.

Received 27th March 2026,
Accepted 19th May 2026

DOI: 10.1039/d6cp01132b

rsc.li/pccp

Introduction

In recent years, the need for a sustainable energy transition toward renewable sources like sunlight has motivated growing interest in innovative photovoltaic devices. Metal halide perovskites (MHPs) have been extensively evaluated as promising candidates for different optoelectronic technologies.[1–6] This interest is largely driven by their remarkable properties, including high absorption coefficients, efficient charge transport, long carrier lifetimes, and a tunable bandgap.[7–10] Among MHPs, lead-based systems are the most exploited for a wide range of applications.[11–14] Notably, they currently achieve the highest power conversion efficiencies (PCEs), rivaling those of commercial silicon-based solar cells,[15] and they also demonstrate very promising performance in photocatalytic processes.[16,17] However, the commercialization and large-scale applications of lead-based perovskites are hindered by their limited stability under environmental conditions and the high toxicity of lead, which poses significant environmental and health concerns.[18]

To address these challenges, the search for lead-free alternatives has become a primary focus in the field of photoconversion devices. Specifically, in the field of photocatalysis, new devices must have a strong response to visible light, a highly active surface for redox reactions and efficient charge separation.[19,20] One promising direction is the substitution of lead with bismuth.[21,22] Bismuth-based systems offer an attractive pathway to develop lead-free perovskites, as bismuth's trivalent nature enables the formation of defect-tolerant perovskite structures known as defect-ordered perovskites.[23–25] While these bismuth-based materials maintain a structural resemblance to MHPs through shared-corner octahedra (MX_6), they adopt unique configurations due to cation deficiencies inherent in their design. Specifically, bismuth forms structures of the type **$A_3M_2X_9$**, where vacancies in the cation lattice result in the occupation of only two-thirds of the M sites.[26] This structure has been shown to promote both stability and defect tolerance in ways distinct from lead-based perovskites, making these bismuth-based halides a promising avenue for further investigation.[27,28]

Perovskite-inspired materials[29–31] like **$Cs_3Bi_2I_9$** and **$Cs_3Bi_2Br_9$** have recently been successfully applied in photovoltaic devices.

[a] Department of Physics "E. Pancini", University of Naples Federico II, Naples, 80126, Italy. E-mail: anabelen.munozgarcia@unina.it
[b] Department of Civil, Environmental, Land, Construction and Chemistry, Polytechnic University of Bari, Bari, 70125, Italy
[c] Department of Chemical Sciences, University of Naples Federico II, Naples, 80126, Italy

The iodine-based compound $Cs_3Bi_2I_9$ has been extensively utilized in photocatalysis, particularly in applications such as dye degradation,[32] the hydrogen evolution reaction (HER),[33,34] and CO_2 reduction.[32–37] Beyond their intrinsic photocatalytic activity, these materials are also attractive as light-harvesting antenna systems due to their strong solar absorption capabilities, enabling efficient photoinduced charge transfer toward the catalytically active material, as previously reported in related photocatalytic systems.[38,39] In this context, we propose the use of these compounds primarily as antenna materials to enhance solar light harvesting and promote charge separation and transfer toward the catalytic sites.

However, the inherent low dimensionality of the $Cs_3Bi_2I_9$ system significantly limits its efficiency across these applications.[40,41] The bromine-based compound $Cs_3Bi_2Br_9$ has also demonstrated considerable potential in photocatalytic applications.[42–45] However, its large band gap and high exciton binding energy impose constraints on its performance, particularly under visible light irradiation.[26] Despite these challenges, its structural and optoelectronic properties suggest that it could be optimized for improved performance in targeted applications.

Given these limitations, it is critical to explore strategies to enhance the efficiency of these materials: one promising strategy involves tuning the halide composition of these systems, which has been shown to effectively modify their electronic properties and optimize their functionality.[46] For example, it has been demonstrated that the mixing of similar halides (I–Br, Cl–Br) in these compounds increases the system's dimensionality, leading to a substantial improvement in optoelectronic properties and photocatalytic activity.[47–49]

From a theoretical perspective, research efforts have primarily focused on characterizing the structural and electronic properties of these systems. These studies have emphasized analyses of band structure, density of states, and, in certain cases, charge transport properties through effective mass calculations.[50–52] However, most of these investigations have been restricted to pure systems, specifically $Cs_3Bi_2I_9$ and $Cs_3Bi_2Br_9$, leaving a break in understanding the impact of halogen mixing on these properties across varying compositions. Moreover, the influence of halogen substitution on the structural properties of these materials has not been systematically analyzed.

Previous experimental studies have reported a compositional phase stability crossover in mixed halide systems occurring at intermediate bromine concentrations (~30–40%), where a transition between competing structural motifs is observed. While these findings establish the existence of the crossover, the underlying microscopic origin driving this behavior remains insufficiently understood. In particular, a quantitative structural description linking local lattice distortions to phase stability across composition is still lacking. In this work, we go beyond the reproduction of this experimentally observed crossover by identifying the structural parameters that govern it. Using first-principles calculations, we systematically analyze the evolution of octahedral distortion metrics, specifically ζ, Σ and θ, as a function of composition. These descriptors provide a quantitative framework to capture subtle local structural changes and enable a direct correlation between local octahedral geometry and the observed phase stability crossover. Our results reveal that the transition is strongly governed by the progressive accumulation and reorganization of octahedral distortions, especially in the Σ and θ parameters, offering a microscopic structural explanation for the experimentally reported phase boundary. To this end, we propose a theoretical study of $Cs_3Bi_2I_9$, $Cs_3Bi_2Br_9$, and mixed-halide systems $Cs_3Bi_2I_{9-x}Br_x$ (with $0 < x < 9$). Our investigation focuses on understanding the effect of relative halogen content on the structure, the electronic profile and the charge transport features. Additionally, we aim to analyze the phase transition between iodine-rich and bromine-rich phases, as well as the degree of distortion induced by varying halide compositions. Our study lays the ground for future work on the application of these materials in both photovoltaic technologies and photocatalysis.

Structural models and computational details

We report all-electron density functional theory calculations with periodic boundary conditions (PBC), employing the light-tier1 basis set of numerical atom-centered orbitals (NAO)[53] for each atom and the zero-order regular approximation (atomic ZORA)[54] as implemented in the Fritz Haber Institute *ab initio* molecular simulations (FHI-aims) code.[55] A self-consistency threshold of 1×10^{-6} eV is set for the total energy. We use the Perdew–Burke–Erzenhof (PBE) exchange correlation functional[56,57] for all geometry optimizations plus the Tkatchenko–Scheffler (TS) correction[58] to take into account the van der Waals forces. Our relaxed structures present maximum forces acting on each atom below 0.02 eV $Å^{-1}$. For the unit cell optimizations, we employ a $4 \times 4 \times 2$ and $4 \times 4 \times 4$ *k*-point grid for $Cs_3Bi_2I_9$ and $Cs_3Bi_2Br_9$, respectively. Based on the optimized geometry, we have calculated the system's energy using the HSE06 hybrid functional and the TS correction.

We compute the band structure and density of states (DOS) by increasing the basis set to an intermediate–tier2 basis set and using finer *k*-point grids for Brillouin zone sampling ($12 \times 12 \times 6$ and $12 \times 12 \times 12$ for the I-based and Br-based compounds, respectively). The hybrid functional HSE06[59,60] and spin orbit coupling (SOC) relativistic correction are employed to achieve a more accurate description of the electronic properties.

To simulate the mixed halide compositions, we adopt a supercell approach considering a $2 \times 1 \times 1$ supercell for $Cs_3Bi_2I_9$ and a $2 \times 1 \times 2$ supercell for $Cs_3Bi_2Br_9$. Both supercells contain a total of 56 atoms. Mixed composition supercells are generated by systematically increasing the bromine content in the iodine-based supercell through substitutions. Similarly, iodine is introduced incrementally into the bromine-based supercell. We consider for both phases the 0, 11, 19, 31, 39, 50, 61, 69, 81, 89 and 100 doping percentages corresponding to substitutions of 0, 4, 7, 11, 14, 18, 22, 25, 29, 32, and 36 halogen atoms. In this work, the SQSs were generated using the *sqsgen* code.[61,62] The configurational space was explored using the systematic iteration mode, in which atomic permutations are generated in

lexicographical order. Unlike the random mode, this approach ensures a deterministic and exhaustive scan of the configurational space; consequently, the number of iterations is not user-defined but fixed by the total number of possible configurations, given by:

$$N_{\text{iterations}} = \frac{N!}{\prod_{m=1}^{M} N_m!}, \quad \text{with} \sum_{m=1}^{M} N_m = N,$$

where N is the total number of atoms, M the number of species, and N_m the number of atoms of each species. To ensure convergence of the correlation functions toward those of an ideal random alloy, we included pair correlations up to the ninth coordination shell (first core shell = 9) and the sixth shell for higher-order correlations (second core shell = 6). Additionally, a shell-weighting scheme was employed to account for the decreasing importance of more distant coordination shells in the objective function.

The mixed-composition systems are optimized at the same level of theory as the unit cells, and the k-point grids are adjusted accordingly to the larger supercells. For the optimized structures with mixed compositions, the electronic properties have been investigated through DOS, band structures calculated at the HSE06 level of theory. In this work, the effective masses were computed using the effmass package[63] by fitting the band dispersion in the vicinity of the band extrema (VBM and CBM). The software evaluates the curvature of the bands and provides effective mass values based on these fits. The effective masses were extracted using a parabolic fit within a k-range of $\pm$0.5 eV around the band extrema. This range was chosen to ensure that the fitting is restricted to the near-edge region where the band dispersion can be reasonably approximated as parabolic, while avoiding numerical noise from an excessively narrow window. Since the band dispersion near the extrema is relatively isotropic in our systems, we report averaged effective mass values as obtained directly from the code. These values correspond to an effective representation of the carrier mass and are suitable for capturing the overall transport trends discussed in this study.

Results and discussion

Structural properties of $Cs_3Bi_2X_9$ compounds and phase stability

Regarding the unit cells of pristine **$Cs_3Bi_2I_9$** and **$Cs_3Bi_2Br_9$**, for the first compound, we consider the hexagonal phase (space group $P6_3/mmc$ (194)),[64] while for **$Cs_3Bi_2Br_9$**, the trigonal phase (space group $P\text{-}3m1$ (164)),[65] which are the most stable at room temperature. Fig. 1a and b depict the main structural parameters of the PBE-TS optimized structures, with the corresponding experimental values reported for comparison.

In both cases, the lattice parameters and bond distances reproduce quite well the experimental values, with just small discrepancies. We investigate the phase stability between the $P6_3/mmc$ phase of the **$Cs_3Bi_2I_9$** and the $P\text{-}3m1$ phase of **$Cs_3Bi_2Br_9$** upon bromine doping and the local distortions of Bi–halogen octahedra. To this end, we consider for each phase a 56 atom supercell (Fig. 1a and b) and we simulate different percentages of I/Br doping ranging from 0% to 100%. The results of these analyses are shown in Fig. 1c–e. The phase stability is evaluated through calculations of relative electronic energy differences between the two phases at different I/Br ratios. Fig. 1c depicts a plot of energy differences between **$Cs_3Bi_2I_9$** in the $P6_3/mmc$

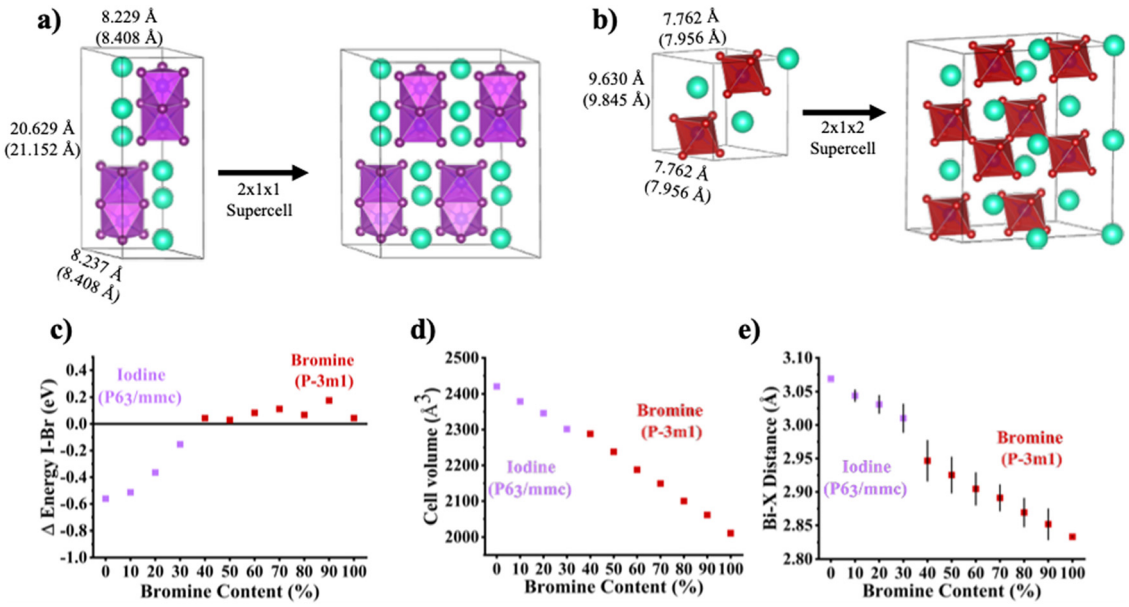

Fig. 1 Lattice constants calculated at PBE-TS level of theory for: (a) **$Cs_3Bi_2I_9$** and (b) **$Cs_3Bi_2Br_9$**. The corresponding experimental values are reported in parenthesis. (c) Total energy differences between **$Cs_3Bi_2I_9$** *in the* $P6_3/mmc$ phase at various Br doping percentages and the corresponding **$Cs_3Bi_2Br_9$** $P\text{-}3m1$ phase with the same I/Br ratio ($\Delta E = E(P6_3/mmc) - E(P\text{-}3m1)$). Energies are calculated at HSE06-TS on top of PBE-TS optimized structures, (d) cell volume and (e) average distance Bi–halogen with error bars calculated through standard deviation.

phase (at various Br doping percentages) and the corresponding **$Cs_3Bi_2Br_9$** *P*-3*m*1 phase (with the same I/Br ratio), calculated using minimum-energy structures, which are shown in Fig. S1 in the SI. These results show that systems with low bromine concentration (range 0%–30%) exhibit negative energy difference values, indicating the $P6_3/mmc$ phase as the most stable phase at these compositions. Beyond this range we obtain positive values, indicating that the starting iodine phase is no longer the most stable configuration. The change point predicted by our calculations is very close to the available experimental values.[66,67]

Moreover, we observe a decrease in the cell volume (Fig. 1d) as the percentage of bromine in the cell increases. This is attributed to the difference in Bi–halide bond distances between I and Br. The bond distance of 3.07 Å in the pure iodine-based system decreases to 2.83 Å in the pure bromine-based system (Fig. 1e), this expected behaviour can be attributed to iodine's larger ionic radius compared to bromine.

Once the phase stability at each point has been identified, we aim at identifying the structural parameters acting as key descriptors for the phase transition. We first considered the structural changes in the **$Cs_3Bi_2I_9$** in the $P6_3/mmc$ phase at varying bromine content: the selected parameters for our study are (1) the Bi–X distances, (2) the cell volume variations upon doping, and (3) three specific parameters describing the local octahedral distortions (evaluated with the Octadist software).[68] These three parameters are the stretching (ζ), the angular (Σ) and the torsional (θ) distortions, calculated according to eqn (1)–(3).

$$\zeta = \sum_{i=1}^{6} |d_i - d_{\text{mean}}| \quad (1)$$

The ζ parameter is the addition of the average of the total differences between six distinct metal–ligand bond lengths (d_i) and their mean bond length around the central metal atom (d_{mean}).

$$\Sigma = \sum_{i=1}^{6} |\phi_i - 90| \quad (2)$$

where ϕ_i is the individual *cis* angle. The parameter Σ represents the total deviation of 12 distinct *cis* ligand–metal–ligand angles (ϕ_i) from 90°.

$$\Theta = \sum_{i=1}^{6} |\theta_i - 60| \quad (3)$$

where θ_i is the individual angle between two vectors of two twisting faces. The parameter Θ is defined as the degree of trigonal distortion of the coordination geometry from an octahedron towards a trigonal prism. This parameter is the sum of the deviation of 24 unique torsional angles between the ligand atoms on opposite triangular faces of the octahedron viewed along the pseudo-threefold axis (θ_i) from 60°. The corresponding equations and graphical representation of these parameters are all shown in Fig. 2a–c.

Analysis of the distortion metrics ζ, Σ, and θ (Fig. 2a–c) reveals a general increase in octahedral distortion as the bromine content rises, with Σ and θ showing the most pronounced compositional sensitivity. In contrast, ζ displays only minor variation across the full composition range, spanning approximately 0.45 to 0.80 Å, suggesting that this parameter cannot be the primary descriptor of halide-dependent deformation in this system.

For Σ and θ, a slight reduction in distortion is observed at 10% Br incorporation. Although modest, this composition coincides with the Br content at which Li and co-workers[69] reported a maximum in charge-carrier mobility, which they attributed to a phase transition. In contrast, our structural analysis indicates that the phase change occurs at higher Br contents (≈30%). In this context, the reduced distortion at 10% Br could be compatible with an enhancement of charge-carrier mobility, potentially preceding the phase transition. Beyond this point, distortion increases steadily up to ~40% Br, coinciding with the shift in thermodynamic preference from the $P6_3/mmc$ phase to the *P*-3*m*1 phase. Once the *P*-3*m*1 phase dominates, the distortion plateaus between 40% and 70% Br and ultimately reaches its maximum between 80% and 100% Br.

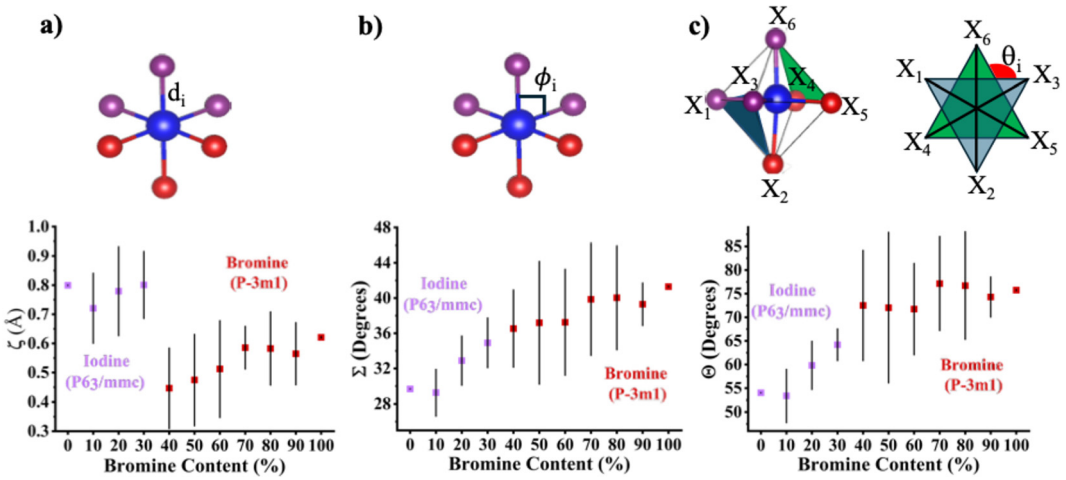

Fig. 2 Variation of the structural parameters evaluated on **$Cs_3Bi_2I_9$** in the $P6_3/mmc$ phase at different Br contents with error bars calculated through standard deviation for the (a) stretching (ζ), (b) the angular (Σ) and (c) the torsional (θ) distortions.

The stronger distortion in Br-rich compositions likely arises from their predominant 2D octahedral connectivity, which imposes cooperative tilting and bond-angle adjustments across extended layers. This contrasts with the 0D dimeric arrangement that is characteristic of the I-rich end of the series, where geometric relaxation is more localized and distortion is correspondingly reduced. The observed trend in octahedral distortion appears to facilitate the mechanisms necessary for understanding the phase stability, thereby influencing the overall physical and chemical properties of the system. These findings show a strong correlation between structural distortion and phase stability trends.

Electronic and transport properties of $Cs_3Bi_2X_9$ compounds

We characterize the electronic structure of the investigated compounds with band structure calculations and projected density of states (pDOS). We have tested different combinations of basis sets and functionals to find the best performing level of theory for accurately predicting the electronic features of these compounds. We also performed some tests accounting for the relativistic spin orbit coupling (SOC) correction, which can be important when dealing with heavy atoms like Bi and late halides. Bandgaps obtained for the two pristine single phases with different basis set/functional choices are reported in Table 1.

Results suggest an underestimation of the experimental values when using the PBE functional with the light basis set. On the other hand, increasing the basis set size while keeping the same functional leads to an overestimation of the bandgaps for both compounds. The best results are obtained with the hybrid HSE06 functional with intermediate basis set and by accounting SOC. The use of SOC probably decreases the energy of the CB populated by the Bi state, the most affected by SOC, together with halogen states. For these reasons, the electronic structure is investigated at this level of theory, considering denser *k*-point grids for the two compounds, namely 12 × 12 × 12 and 12 × 12 × 6 for Br- and I-based compounds, respectively. This approach strikes a good balance between accuracy and computational cost without resorting to more sophisticated methods like G_0W_0.[70]

Table 1 Band gap values calculated with different basis sets/functional choices for the pure phases of the single halogen compounds. In all calculations, 12 × 12 × 6 and 12 × 12 × 12 *k*-point grids are used for I- and Br-based compounds, respectively. Experimental values are reported in the last row for comparison

	Bandgaps (eV)	
Basis set/Functional	$Cs_3Bi_2I_9$	$Cs_3Bi_2Br_9$
Light/PBE	1.80	2.30
Intermediate/PBE	2.31	2.95
Light/HSE06	2.32	2.95
Intermediate/HSE06 + SOC	2.15	2.48
Experimental	2.00[66,71]	2.64[66,72]

Fig. 3a displays the band structure calculated for the $Cs_3Bi_2I_9$ system along the high-symmetry *k*-point path: Γ (0, 0, 0), M (0.5, 0, 0), K (0.333, 0.333, 0), Γ (0, 0, 0), A (0, 0, 0.5), L (0.5, 0, 0.5), H (0.333, 0.333, 0.5), A (0, 0, 0.5), M (0.5, 0, 0), H (0.333, 0.333, 0.5). The results indicate that the system exhibits an indirect bandgap with a value of 2.14 eV, occurring between the Γ → K points. These findings are consistent with previously reported results for the same material.[50,73,74]

For the $Cs_3Bi_2Br_9$ system, the *k*-path includes the same high-symmetry points as the previous system. As shown in Fig. 3b, this system also exhibits an indirect bandgap (2.48 eV), occurring between a point in the K–Γ segment and the A point, aligning with previously reported findings.[75,76]

The analysis of the projected density of states (*p*DOS), also reported in Fig. 3, indicates the significant participation of the halogen orbitals (Br and I) in the region of the occupied bands. In the region of the unoccupied bands, there is evidence of a notable contribution of both bismuth and halogen atoms, with bismuth having a greater participation in the bands close to the Fermi level. This behavior suggests a strong hybridization between the orbitals of these atoms. This interaction contributes to the stability of the bond and affects the optical and electronic properties of the material, making it relevant for various technological applications.

We calculate the band gap and effective masses for holes and electrons at varying bromine content using the same level of theory. The results for these properties are presented in Fig. 4: the band-gap data exhibit an almost linear increase with bromine incorporation. At the atomistic level, the band gap increases when Br substitutes I mainly because of the different

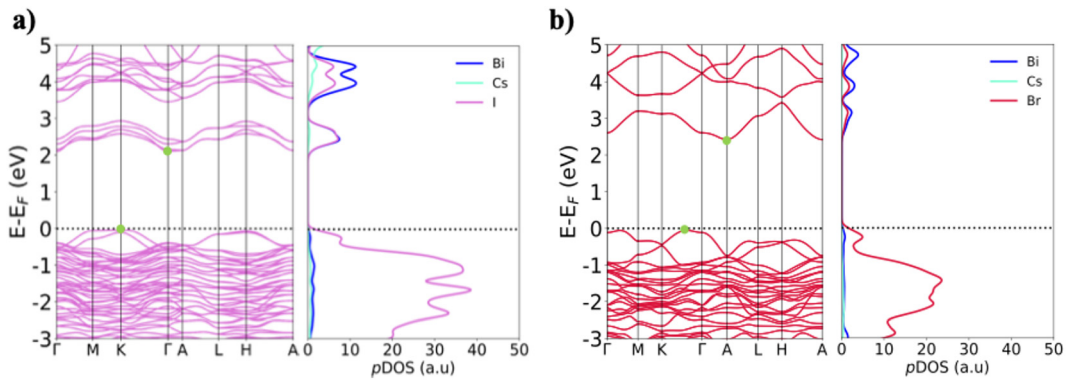

Fig. 3 Band structure calculated at HSE06 + SOC level of theory for (a) $Cs_3Bi_2I_9$ and (b) $Cs_3Bi_2Br_9$. Green circles connect points in which the VBM to CBM transition is observed.

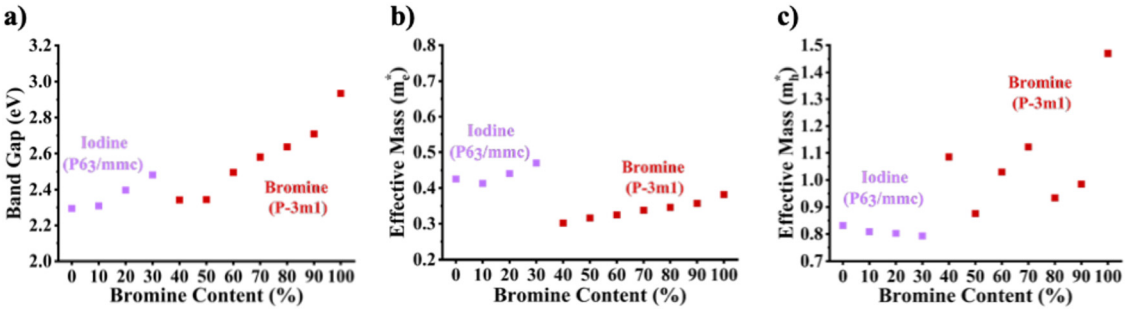

Fig. 4 (a) Bandgap values calculated at HSE06 level of theory in all the mixed halide compositions investigated. Electron (b) and hole (c) effective masses calculated from band structures of the mixed I/Br systems, within the parabolic band approximation. Masses are referred to the rest mass of the electron.

electronic character of the halogen p orbitals. In $\mathbf{Cs_3Bi_2I_9}$, the valence band maximum (VBM) is largely dominated by I-5p orbitals, which are relatively high in energy due to iodine's lower electronegativity and larger size. When I is replaced by Br, these are substituted with Br-4p orbitals, which are lower in energy because bromine is more electronegative and its orbitals are more tightly bound. As a result, the VBM shifts downward (to lower energy). The conduction band minimum (CBM), mainly derived from Bi-6p states, is much less affected. This asymmetric shift leads to an overall widening of the band gap. In short, replacing I with Br stabilizes (lowers) the valence band due to deeper Br-p orbitals. We also found a marked decrease near 40% Br that cannot be explained by a simple compositional trend. This deviation originates from the fact that the $Cs_3Bi_2X_9$ system does not maintain a single crystallographic framework across the full halide range. At intermediate compositions, the material lies at the boundary between the 0D dimer-based structure and the layered 2D structure, and the optimized geometries at these ratios inevitably relax toward different structural minima. Because these configurations possess intrinsically distinct electronic structures, particularly in terms of dimensionality, orbital overlap, and Bi–X connectivity, the band gaps extracted in this regime effectively represent two different phases rather than a continuous solid solution. The apparent reduction in band gap is therefore not an intrinsic bowing effect but a consequence of sampling mixed-phase configurations, reflecting a change in the dominant structural motif rather than any anomalous electronic behavior. We note that the stronger band gap bowing reported for nanocrystals by Ghosh for is likely enhanced by quantum confinement effects, whereas our calculations correspond to the bulk limit.[40]

Effective mass of the electrons and holes

Effective masses are very useful quantities to assess the charge carrier transport in a system. Hole and electron's effective masses can be estimated, within a parabolic band approximation, through the following expression:

$$m_i^* = \hbar^2 \left[\frac{\partial^2 \varepsilon(k)}{\partial k^2} \right]^{-1} \quad (4)$$

where $\hbar$ is the reduced Planck constant, k is the wavevector in different directions, and $\varepsilon(k)$ represents the energy of the valence and conduction bands for holes and electrons, respectively. The values of $\frac{\partial^2 \varepsilon(k)}{\partial k^2}$ are estimated from the band structure plots (Fig. S2) using the finite differences fit technique, as implemented in the *effmass* software package.[63] The analysis of the band structure reveals that both systems exhibit much flatter valence band maxima (VBM) compared to their conduction band minima (CBM). This observation suggests that holes are likely to have higher effective masses and be more localized than electrons.

The average effective masses along the different k-directions of the holes are $0.831m_h^*$ and $1.017m_h^*$ y for the I and Br systems, respectively, while the corresponding values for electrons are $0.424m_e^*$ and $0.385m_e^*$ for I and Br systems, respectively. These findings indicate that both materials exhibit a higher mobility for electrons compared to hole mobility. Our results align well with previously reported values in the literature,[34,51,77,78]

We calculate the hole and electron effective masses for each composition, *i.e.* we start from the pure Iodine phase and calculate the effective masses at varying Br percentage. The values for the electron effective masses (Fig. 4b) are similar for all evaluated compositions ranging from 0.29 to 0.47. This behavior aligns with expectations, given that the conduction band is not significantly influenced by the halogen species.

Conversely, the hole effective masses (Fig. 4c) exhibit a pronounced increase beyond 40% Br content. This behavior is intrinsically linked to the electronic structure of the material: for Br contents below 40%, the valence band is predominantly composed of iodine-derived orbitals, whereas at higher Br concentrations, bromine orbitals become dominant (Fig. S2). The observed increase in hole effective mass can be attributed to the strong self-trapping of photogenerated holes by Br atoms, an effect that has been previously documented in the literature.[79] This phenomenon underscores the impact of halogen substitution on the electronic transport properties, particularly in the context of charge localization and mobility, which are critical factors for the performance of optoelectronic applications.

In recent studies, two specific compositions have been predominantly highlighted as optimal for charge transport in Cs-based bismuth halide perovskites. Sun *et al.*[47] identified $Cs_3Bi_2I_6Br_3$ as the most effective structure for charge transport, while more recently, Li *et al.*[69] reported that $Cs_3Bi_2I_8Br_1$ exhibits superior electron mobility among the studied compositions.

Here, we identify two compositions with the lowest and closely matched effective masses for charge carriers (Fig. 4c), occurring at 10% and 30% Br content, respectively. These values are consistent with the aforementioned experimental findings. Li *et al.* attributed the increase in effective mass to a phase transition, which we also predict indirectly; however, in our case, this occurs at approximately 30% Br content, as mentioned earlier. The improvement in mobility could be related to a slight decrease in distortion parameters. Our observation of a change in phase stability order aligns more closely with the composition reported by Sun *et al.*, as well as with other experimental studies that have documented a phase transition near 30% Br content. These results demonstrate the importance not only of the phase but also of the system's composition, and the structural changes that occur within the system at each composition, which broadly determine the electronic and optical properties of this material.

Conclusions

Here we report a first-principles investigation on the structural and electronic properties of the endpoint compounds $\mathbf{Cs_3Bi_2I_9}$ and $\mathbf{Cs_3Bi_2Br_9}$, promising materials for photovoltaic and photocatalytic applications, and of their iodine–bromine solid solution. In particular, we address the role of halogen mixing as a strategy for tuning their electronic features for potential optoelectronic applications. We focus specifically on the phase equilibria upon halogen mixing and our calculations predict a change in phase stability order at about 30% bromine doping, with the iodine phase ($P6_3/mmc$) being most stable below 30% Br, while the bromine phase ($P\text{-}3m1$) dominating beyond 40% Br, in agreement with recent experimental findings.[66,67] A thorough structural analysis allows assessing the octahedral distortion as the main structural parameter acting as driving force for the phase transition. We observe a decrease of the Bi–X bond length with increasing Br content, leading to a decrease of the unit cell volume.

While our results are consistent with experimentally reported phase stability crossover at intermediate Br concentrations ($\sim$30–40%), the primary contribution of this work lies in providing a microscopic structural interpretation of this behavior. In particular, we demonstrate that octahedral distortion descriptors (ζ, Σ, and θ) serve as robust quantitative indicators of structural instability and play a central role in driving the phase transition. The systematic evolution of these parameters with composition reveals a clear structural mechanism underlying the crossover, rather than a purely compositional effect. This establishes a direct link between local geometric distortions and macroscopic phase behavior.

More broadly, our findings highlight octahedral distortion metrics as general predictive descriptors for phase stability in halide-based materials, providing a framework that may be extended to related systems where subtle structural effects govern phase competition.

The electronic structures of both the pure $\mathbf{Cs_3Bi_2I_9}$ and $\mathbf{Cs_3Bi_2Br_9}$ exhibit indirect band gaps, with values of 2.14 eV and 2.48 eV, respectively, obtained using the HSE06 hybrid functional including spin–orbit coupling (SOC). These results align closely with experimental values and highlight the importance of incorporating SOC for systems containing heavy elements like bismuth. The significant contribution of SOC to the electronic structure, especially in the conduction band, emphasizes its necessity for accurately describing relativistic effects in such materials. The projected density of states (pDOS) analysis reveals strong hybridization between the orbitals of bismuth and halogen atoms, which significantly influences the materials' stability as well as their physico–chemical properties. The valence band is dominated by halogen orbitals, while the conduction band shows contributions from both bismuth and halogens, with bismuth playing a prominent role near the Fermi level. This hybridization not only stabilizes the crystal structure but also enhances its potential for optoelectronic applications.

The bandgap is also affected by changes in the bromine content, and we find a correlation of the bandgap trend with the experimental data, with the band gap increasing with Br content, except during the transitional phase (40–50%Br).

Regarding charge transport in the two materials and the effect of halogen mixing on the effective masses of charge carriers, our band structure calculations reveal that both systems exhibit flatter valence band maxima (VBM) compared to their conduction band minima (CBM), suggesting that holes are more localized and exhibit higher effective masses than electrons, which indicates significantly greater electron mobility than hole mobility in both materials. In other words, the low effective masses of electrons imply that they are less localized and can contribute more effectively to charge transport, which is a key feature for various applications. Effective mass analysis shows nearly constant electron masses across compositions, while hole masses increase beyond 50% Br due to self-trapping by Br atoms.[79,80]

Overall, our findings highlight the impact of halogen composition on structural, electronic, and transport properties, offering valuable insights for tuning material properties in halide perovskite-inspired materials for different potential optoelectronic applications.

Conflicts of interest

There are no conflicts of interest to declare.

Data availability

The data supporting this article have been included as part of the supplementary information (SI). Supplementary information: supercells used for modeling different the Br/I compositions and corresponding electronic band structures and PDOS. See DOI: https://doi.org/10.1039/d6cp01132b.

Acknowledgements

We acknowledge financial support under the National Recovery and Resilience Plan (NRRP), Mission 4, Component 2, Investment 1.1, Call for Tender No. 1409, published on 14.9.2022 by the Italian Ministry of University and Research (MUR), funded

by the European Union – NextGenerationEU – Project Title: Boosting CO_2 conversion with Multilayer Bifunctional photocatalysts (BOMBCAT) – CUP E53D23015580001 – Grant Assignment Decree No. 1386, adopted on 01.09.2023 by the Italian Ministry of University and Research (MUR). The computing resources and the related technical support used for this work have been provided by CRESCO/ENEAGRID High-Performance Computing infrastructure and its staff.[81] CRESCO/ENEAGRID High-Performance Computing infrastructure is funded by ENEA, the Italian National Agency for New Technologies, Energy and Sustainable Economic Development, and by Italian and European research projects; see https://www.cresco.enea.it/english for further information. The authors also acknowledge the extensive use of the ENEA FARO facility and the support of its management team.[82]

References

1 Z.-Y. Chen, N.-Y. Huang and Q. Xu, Metal halide perovskite materials in photocatalysis: Design strategies and applications, *Coord. Chem. Rev.*, 2023, **481**, 215031.
2 K. Ren, S. Yue, C. Li, Z. Fang, K. A. M. Gasem, J. Leszczynski, S. Qu, Z. Wang and M. Fan, Metal halide perovskites for photocatalysis applications, *J. Mater. Chem. A*, 2022, **10**, 407–429.
3 W. Xiang, S. (Frank) Liu and W. Tress, A review on the stability of inorganic metal halide perovskites: challenges and opportunities for stable solar cells, *Energy Environ. Sci.*, 2021, **14**, 2090–2113.
4 H. Dong, C. Ran, W. Gao, M. Li, Y. Xia and W. Huang, Metal Halide Perovskite for next-generation optoelectronics: progresses and prospects, *eLight*, 2023, **3**, 3.
5 G. V. Sannino, A. Pecoraro, P. Maddalena, A. Bruno, P. D. Veneri, M. Pavone and A. B. Muñoz-García, The role of Mg dopant concentration in tuning the performance of the SnO_2 electron transport layer in perovskite solar cells, *Sustainable Energy Fuels*, 2023, **7**, 4855–4863.
6 A. Pecoraro, P. Maddalena, M. Pavone and A. B. Muñoz García, First-Principles Study of Cu-Based Inorganic Hole Transport Materials for Solar Cell Applications, *Materials*, 2022, **15**, 5703.
7 Y. Zhou, I. Poli, D. Meggiolaro, F. De Angelis and A. Petrozza, Defect activity in metal halide perovskites with wide and narrow bandgap, *Nat. Rev. Mater.*, 2021, **6**, 986–1002.
8 T. Niu, J. Lu, R. Munir, J. Li, D. Barrit, X. Zhang, H. Hu, Z. Yang, A. Amassian, K. Zhao and S. (Frank) Liu, Stable High-Performance Perovskite Solar Cells via Grain Boundary Passivation, *Adv. Mater.*, 2018, **30**, 1706576.
9 L. Lei, Q. Dong, K. Gundogdu and F. So, Metal Halide Perovskites for Laser Applications, *Adv. Funct. Mater.*, 2021, **31**, 2010144.
10 Z. Liu, L. Qiu, L. K. Ono, S. He, Z. Hu, M. Jiang, G. Tong, Z. Wu, Y. Jiang, D.-Y. Son, Y. Dang, S. Kazaoui and Y. Qi, A holistic approach to interface stabilization for efficient perovskite solar modules with over 2000-hour operational stability, *Nat. Energy*, 2020, **5**, 596–604.
11 S. Zhao, S. Jin, H. Liu, Y. Su, W. Liu, S. Li, C. She, H. Li and K. Chen, Bandgap Engineering for Photocatalytic Polymerization of 3, 4-Ethylenedioxythiophene (EDOT) over $Cs_3Bi_xSb_{(2-x)}Br_9$ Inverse Opals, *ChemCatChem*, 2022, **14**, e202101539.
12 A. J. Lehner, D. H. Fabini, H. A. Evans, C.-A. Hébert, S. R. Smock, J. Hu, H. Wang, J. W. Zwanziger, M. L. Chabinyc and R. Seshadri, Crystal and Electronic Structures of Complex Bismuth Iodides $A_3Bi_2I_9$ (A = K, Rb, Cs) Related to Perovskite: Aiding the Rational Design of Photovoltaics, *Chem. Mater.*, 2015, **27**, 7137–7148.
13 A. Johnston, F. Dinic, P. Todorović, B. Chen, L. K. Sagar, M. I. Saidaminov, S. Hoogland, O. Voznyy and E. H. Sargent, Narrow Emission from Rb_3 Sb_2 I_9 Nanoparticles, *Adv. Opt. Mater.*, 2020, **8**, 1901606.
14 A. Pecoraro, F. Fasulo, M. Pavone and A. B. Muñoz-García, First-principles study of interfacial features and charge dynamics between spiro-MeOTAD and photoactive lead halide perovskites, *Chem. Commun.*, 2023, **59**, 5055–5058.
15 W. S. Yang, J. H. Noh, N. J. Jeon, Y. C. Kim, S. Ryu, J. Seo and S. I. Seok, High-performance photovoltaic perovskite layers fabricated through intramolecular exchange, *Science*, 2015, **348**, 1234–1237.
16 X. Zhu, Y. Lin, J. San Martin, Y. Sun, D. Zhu and Y. Yan, Lead halide perovskites for photocatalytic organic synthesis, *Nat. Commun.*, 2019, **10**, 2843.
17 Y.-H. Chen, J.-K. Ye, Y.-J. Chang, T.-W. Liu, Y.-H. Chuang, W.-R. Liu, S.-H. Liu and Y.-C. Pu, Mechanisms behind photocatalytic CO_2 reduction by $CsPbBr_3$ perovskite-graphene-based nanoheterostructures, *Appl. Catal., B*, 2021, **284**, 119751.
18 B. Conings, J. Drijkoningen, N. Gauquelin, A. Babayigit, J. D'Haen, L. D'Olieslaeger, A. Ethirajan, J. Verbeeck, J. Manca, E. Mosconi, F. D. Angelis and H. Boyen, Intrinsic Thermal Instability of Methylammonium Lead Trihalide Perovskite, *Adv. Energy Mater.*, 2015, **5**, 1500477.
19 X. Li, J. Yu, M. Jaroniec and X. Chen, Cocatalysts for Selective Photoreduction of CO_2 into Solar Fuels, *Chem. Rev.*, 2019, **119**, 3962–4179.
20 K. Li, B. Peng and T. Peng, Recent Advances in Heterogeneous Photocatalytic CO_2 Conversion to Solar Fuels, *ACS Catal.*, 2016, **6**, 7485–7527.
21 B. Ghosh, B. Wu, H. K. Mulmudi, C. Guet, K. Weber, T. C. Sum, S. Mhaisalkar and N. Mathews, Limitations of $Cs_3Bi_2I_9$ as Lead-Free Photovoltaic Absorber Materials, *ACS Appl. Mater. Interfaces*, 2018, **10**, 35000–35007.
22 H. T. Ramolahloane, G. B. Nair and H. C. Swart, Controlled synthesis and photoluminescence study of blue-emitting $Cs_3Bi_2Br_9$ nanocrystals prepared by the ligand-assisted reprecipitation (LARP) method, *Mater. Res. Bull.*, 2023, **165**, 112285.
23 A. E. Maughan, A. M. Ganose, A. M. Candia, J. T. Granger, D. O. Scanlon and J. R. Neilson, Anharmonicity and Octahedral Tilting in Hybrid Vacancy-Ordered Double Perovskites, *Chem. Mater.*, 2018, **30**, 472–483.
24 G. Giovilli, B. Albini, V. Grisci, S. Bonomi, M. Moroni, E. Mosconi, W. Kaiser, F. De Angelis, P. Galinetto and L. Malavasi, Band gap tuning through cation and halide

alloying in mechanochemically synthesized $Cs_3(Sb_{1-x}Bi_x)_2Br_9$ and $Cs_3Sb_2(I_{1-x}Br_x)_9$ solid solutions, *J. Mater. Chem. C*, 2023, **11**, 10282–10291.

25 X. Chen, M. Jia, W. Xu, G. Pan, J. Zhu, Y. Tian, D. Wu, X. Li and Z. Shi, Recent Progress and Challenges of Bismuth-Based Halide Perovskites for Emerging Optoelectronic Applications, *Adv. Opt. Mater.*, 2023, **11**, 2202153.

26 S. Dai, X. Gan, K. Li, Q. Huang, L. Guo and H. Liu, Bandgap lowering in mixed alloys of $Cs_3Bi_{2-x}Sb_xBr_9$ perovskite powders, *Phys. Chem. Chem. Phys.*, 2023, **25**, 30993–31002.

27 L. Zhang, K. Wang and B. Zou, Bismuth Halide Perovskite-Like Materials: Current Opportunities and Challenges, *ChemSusChem*, 2019, **12**, 1612–1630.

28 X.-G. Zhao, J.-H. Yang, Y. Fu, D. Yang, Q. Xu, L. Yu, S.-H. Wei and L. Zhang, Design of Lead-Free Inorganic Halide Perovskites for Solar Cells via Cation-Transmutation, *J. Am. Chem. Soc.*, 2017, **139**, 2630–2638.

29 B. Al-Anesi, G. K. Grandhi, A. Pecoraro, V. Sugathan, A. B. Muñoz-García, M. Pavone and P. Vivo, Dissecting the Role of the Hole-Transport Layer in Cu_2AgBiI_6 Solar Cells: An Integrated Experimental and Theoretical Study, *J. Phys. Chem. C*, 2024, **128**, 9446–9453.

30 V. Sugathan, M. Liu, A. Pecoraro, T. K. Das, T.-P. Ruoko, G. K. Grandhi, D. Manna, H. Ali-Löytty, K. Lahtonen, A. B. Muñoz-García, M. Pavone and P. Vivo, Halide Engineering in Mixed Halide Perovskite-Inspired Cu_2AgBiI_6 for Solar Cells with Enhanced Performance, *ACS Appl. Mater. Interfaces*, 2024, **16**, 19026–19038.

31 B. Al-Anesi, G. K. Grandhi, A. Pecoraro, V. Sugathan, N. S. M. Viswanath, H. Ali-Löytty, M. Liu, T. Ruoko, K. Lahtonen, D. Manna, S. Toikkonen, A. B. Muñoz-García, M. Pavone and P. Vivo, Antimony-Bismuth Alloying: The Key to a Major Boost in the Efficiency of Lead-Free Perovskite-Inspired Photovoltaics, *Small*, 2023, **19**, 2303575.

32 B.-M. Bresolin, C. Günnemann, D. W. Bahnemann and M. Sillanpää, Pb-Free $Cs_3Bi_2I_9$ Perovskite as a Visible-Light-Active Photocatalyst for Organic Pollutant Degradation, *Nanomaterials*, 2020, **10**, 763.

33 Y. Ji, M. She, X. Bai, E. Liu, W. Xue, Z. Zhang, K. Wan, P. Liu, S. Zhang and J. Li, In-Depth Understanding of the Effect of Halogen-Induced Stable 2D Bismuth-Based Perovskites for Photocatalytic Hydrogen Evolution Activity, *Adv. Funct. Mater.*, 2022, **32**, 2201721.

34 M. Li, S. Xu, L. Wu, H. Tang, B. Zhou, J. Xu, Q. Yang, T. Zhou, Y. Qiu, G. Chen, G. I. N. Waterhouse and K. Yan, Perovskite $Cs_3Bi_2I_9$ Hexagonal Prisms with Ordered Geometry for Enhanced Photocatalytic Hydrogen Evolution, *ACS Energy Lett.*, 2022, **7**, 3370–3377.

35 H. Mai, D. Chen, Y. Tachibana, H. Suzuki, R. Abe and R. A. Caruso, Developing sustainable, high-performance perovskites in photocatalysis: design strategies and applications, *Chem. Soc. Rev.*, 2021, **50**, 13692–13729.

36 O. L. Quintero-Lizárraga, E. Luévano-Hipólito and L. M. Torres-Martínez, A versatile approach for the immobilization of lead-free $Cs_3Bi_2I_9$ perovskites for photocatalytic CO_2 reduction, *J. Phys. Appl. Phys.*, 2023, **56**, 425103.

37 G. Getachew, A. Wibrianto, A. S. Rasal, S. Kizhepat, W. B. Direrssa, V. Gurav and J.-Y. Chang, Lead-free metal halide perovskites as the rising star in photocatalysis: The past, present, and prospective, *Prog. Mater. Sci.*, 2023, **140**, 101192.

38 E. Nikoloudakis, I. López-Duarte, G. Charalambidis, K. Ladomenou, M. Ince and A. G. Coutsolelos, Porphyrins and phthalocyanines as biomimetic tools for photocatalytic H_2 production and CO_2 reduction, *Chem. Soc. Rev.*, 2022, **51**, 6965–7045.

39 Y. Lu, Y. Wang and J. Zhang, Semiconductor heterojunction photocatalysts with near-infrared light antennas: a review, *J. Phys. Appl. Phys.*, 2021, **54**, 313002.

40 S. Ghosh, S. Mukhopadhyay, S. Paul, B. Pradhan and S. K. De, Control Synthesis and Alloying of Ambient Stable Pb-Free $Cs_3Bi_2Br_{9(1-x)}I_{9x}$ $(0 \leq x \leq 1)$ Perovskite Nanocrystals for Photodetector Application, *ACS Appl. Nano Mater.*, 2020, **3**, 11107–11117.

41 M. K. Hossain, G. F. Ishraque Toki, D. P. Samajdar, M. H. K. Rubel, M. Mushtaq, Md. R. Islam, Md. F. Rahman, S. Bhattarai, H. Bencherif, M. K. A. Mohammed, R. Pandey and J. Madan, Photovoltaic Performance Investigation of $Cs_3Bi_2I_9$-Based Perovskite Solar Cells with Various Charge Transport Channels Using DFT and SCAPS-1D Frameworks, *Energy Fuels*, 2023, **37**, 7380–7400.

42 Y. Baghdadi, F. Temerov, J. Cui, M. Daboczi, E. Rattner, M. S. Sena, I. Itskou and S. Eslava, $Cs_3Bi_2Br_9$/g-C_3N_4 Direct Z-Scheme Heterojunction for Enhanced Photocatalytic Reduction of CO_2 to CO, *Chem. Mater.*, 2023, **35**, 8607–8620.

43 A. G. Aragon, T. E. Wiggins, X. Ma and S. M. Geyer, Lead-free Cs3Bi2Br9 and Cs3Bi2_*x*SbxBr9 nanocrystals as photocatalysts with enhanced activity for the degradation of rhodamine in aqueous environments, *J. Photochem. Photobiol., A*, 2023, **436**, 114391.

44 O. Akinbami, R. Moepya, G. N. Ngubeni, P. Tetyana, K. P. Mubiayi, M. J. Moloto and N. Moloto, Lead-free Rudorffite-type $Cs_3Bi_2Br_9$ nanoparticles for photocatalytic degradation of rhodamine B and methylene blue, *J. Photochem. Photobiol., A*, 2021, **419**, 113460.

45 M. Masri, K. B. Girisha, A. Hezam, T. F. Qahtan, K. Alkanad, F. Masri, K. Namratha, Udayabhanu and K. Byrappa, Enhanced photocatalytic activity and stability of 2D $Cs_3Bi_2Br_9$ perovskite nanosheets synthesized via modified antisolvent method, *Colloids Surf., C*, 2024, **2**, 100024.

46 J. Wang, Y. Shi, Y. Wang and Z. Li, Rational Design of Metal Halide Perovskite Nanocrystals for Photocatalytic CO_2 Reduction: Recent Advances, Challenges, and Prospects, *ACS Energy Lett.*, 2022, **7**, 2043–2059.

47 Q. Sun, B. Xiao, L. Ji, D. Zhao, J. Liu, W. Zhang, M. Zhu, W. Jie, B.-B. Zhang and Y. Xu, Effect of dimensional expansion on carrier transport behaviors of the hexagonal Bi-based perovskite crystals, *J. Energy Chem.*, 2022, **66**, 459–465.

48 W. Chen, H. Sun, Y. Jin, H. Yang, Y. He and X. Zhu, Preparation of bismuth-based perovskite Cs3Bi2I6Br3 single crystal for X-ray detector application, *J. Mater. Sci.: Mater. Electron.*, 2023, **34**, 496.

49 J. Kaur and S. Chakraborty, Crossover of Frenkel and Wannier–Mott Excitons Through Halide Composition Tuning in Mixed Halide Perovskites, *Small*, 2025, 2408919.

50 B. Ghosh, S. Chakraborty, H. Wei, C. Guet, S. Li, S. Mhaisalkar and N. Mathews, Poor Photovoltaic Performance of $Cs_3Bi_2I_9$: An Insight through First-Principles Calculations, *J. Phys. Chem. C*, 2017, **121**, 17062–17067.
51 C. Wang, Y. Ding, B. Liu, B. Weng, J. Hofkens and M. B. J. Roeffaers, Crystal structure engineering of metal halide perovskites for photocatalytic organic synthesis, *Chem. Commun.*, 2023, **59**, 3122–3125.
52 Q. Luo, L. Su, Y. Lu, L. Fang, H. Shu, D. Cao and X. Chen, Computational Screening of 2D All-Inorganic Lead-Free Halide Perovskites $A_3B_2X_9$ for Photovoltaic and Photocatalytic Applications, *Adv. Theory Simul.*, 2024, **7**, 2300988.
53 V. Havu, V. Blum, P. Havu and M. Scheffler, Efficient integration for all-electron electronic structure calculation using numeric basis functions, *J. Comput. Phys.*, 2009, **228**, 8367–8379.
54 E. Van Lenthe, A. Van Der Avoird and P. E. S. Wormer, Density functional calculations of molecular hyperfine interactions in the zero order regular approximation for relativistic effects, *J. Chem. Phys.*, 1998, **108**, 4783–4796.
55 V. Blum, R. Gehrke, F. Hanke, P. Havu, V. Havu, X. Ren, K. Reuter and M. Scheffler, Ab initio molecular simulations with numeric atom-centered orbitals, *Comput. Phys. Commun.*, 2009, **180**, 2175–2196.
56 J. P. Perdew, K. Burke and Y. Wang, Generalized gradient approximation for the exchange-correlation hole of a many-electron system, *Phys. Rev. B: Condens. Matter Mater. Phys.*, 1996, **54**, 16533–16539.
57 J. P. Perdew, K. Burke and Y. Wang, Erratum: Generalized gradient approximation for the exchange-correlation hole of a many-electron system [*Phys. Rev. B*, 54, 16533 (1996)], *Phys. Rev. B: Condens. Matter Mater. Phys.*, 1998, **57**, 14999.
58 A. Tkatchenko and M. Scheffler, Accurate Molecular van der Waals Interactions from Ground-State Electron Density and Free-Atom Reference Data, *Phys. Rev. Lett.*, 2009, **102**, 073005.
59 J. Heyd, G. E. Scuseria and M. Ernzerhof, Hybrid functionals based on a screened Coulomb potential, *J. Chem. Phys.*, 2003, **118**, 8207–8215.
60 J. Heyd, G. E. Scuseria and M. Ernzerhof, Erratum: ''Hybrid functionals based on a screened Coulomb potential'' [*J. Chem. Phys.*, **118**, 8207 (2003)], *J. Chem. Phys.*, 2006, **124**, 219906.
61 A. Van De Walle, R. Sun, Q.-J. Hong and S. Kadkhodaei, Software tools for high-throughput CALPHAD from first-principles data, *CALPHAD: Comput. Coupling Phase Diagrams Thermochem.*, 2017, **58**, 70–81.
62 A. Van De Walle, M. Asta and G. Ceder, The alloy theoretic automated toolkit: A user guide, *CALPHAD: Comput. Coupling Phase Diagrams Thermochem.*, 2002, **26**, 539–553.
63 L. D. Whalley, effmass: An effective mass package, *J. Open Source Softw.*, 2018, **3**, 797.
64 Z. Qi, X. Fu, T. Yang, D. Li, P. Fan, H. Li, F. Jiang, L. Li, Z. Luo, X. Zhuang and A. Pan, Highly stable lead-free Cs3Bi2I9 perovskite nanoplates for photodetection applications, *Nano Res.*, 2019, **12**, 1894–1899.
65 T. Geng, S. Wei, W. Zhao, Z. Ma, R. Fu, G. Xiao and B. Zou, Insight into the structure–property relationship of two-dimensional lead-free halide perovskite $Cs_3Bi_2Br_9$ nanocrystals under pressure, *Inorg. Chem. Front.*, 2021, **8**, 1410–1415.
66 S. Bonomi, P. Galinetto, M. Patrini, L. Romani and L. Malavasi, Optical and Structural Property Tuning in Physical Vapor Deposited Bismuth Halides $Cs_3Bi_2(I_{1-x}Br_x)_9$ $(0 \leq x \leq 1)$, *Inorg. Chem.*, 2021, **60**, 14142–14150.
67 B.-B. Yu, M. Liao, J. Yang, W. Chen, Y. Zhu, X. Zhang, T. Duan, W. Yao, S.-H. Wei and Z. He, Alloy-induced phase transition and enhanced photovoltaic performance: the case of $Cs_3Bi_2I_{9-x}Br_x$ perovskite solar cells, *J. Mater. Chem. A*, 2019, **7**, 8818–8825.
68 R. Ketkaew, Y. Tantirungrotechai, P. Harding, G. Chastanet, P. Guionneau, M. Marchivie and D. J. Harding, OctaDist: a tool for calculating distortion parameters in spin crossover and coordination complexes, *Dalton Trans.*, 2021, **50**, 1086–1096.
69 X. Li, G. Zhang, Y. Hua, F. Cui, X. Sun, J. Liu, H. Liu, Y. Bi, Z. Yue, Z. Zhai, H. Xia and X. Tao, Dimensional and Optoelectronic Tuning of Lead-free Perovskite $Cs_3Bi_2I_{9-n}Br_n$ Single Crystals for Enhanced Hard X-ray Detection, *Angew. Chem., Int. Ed.*, 2023, **62**, e202315817.
70 X. Ren, F. Merz, H. Jiang, Y. Yao, M. Rampp, H. Lederer, V. Blum and M. Scheffler, All-electron periodic G_0W_0 implementation with numerical atomic orbital basis functions: Algorithm and benchmarks, *Phys. Rev. Mater.*, 2021, **5**, 013807.
71 Y. Zhang, Y. Liu, Z. Xu, H. Ye, Z. Yang, J. You, M. Liu, Y. He, M. G. Kanatzidis and S. Liu, Nucleation-controlled growth of superior lead-free perovskite $Cs_3Bi_2I_9$ single-crystals for high-performance X-ray detection, *Nat. Commun.*, 2020, **11**, 2304.
72 M. Leng, Y. Yang, K. Zeng, Z. Chen, Z. Tan, S. Li, J. Li, B. Xu, D. Li, M. P. Hautzinger, Y. Fu, T. Zhai, L. Xu, G. Niu, S. Jin and J. Tang, All-Inorganic Bismuth-Based Perovskite Quantum Dots with Bright Blue Photoluminescence and Excellent Stability, *Adv. Funct. Mater.*, 2018, **28**, 1704446.
73 L. Zhang, C. Liu, L. Wang, C. Liu, K. Wang and B. Zou, Pressure-Induced Emission Enhancement, Band-Gap Narrowing, and Metallization of Halide Perovskite $Cs_3Bi_2I_9$, *Angew. Chem., Int. Ed.*, 2018, **57**, 11213–11217.
74 M. Pazoki, M. B. Johansson, H. Zhu, P. Broqvist, T. Edvinsson, G. Boschloo and E. M. J. Johansson, Bismuth Iodide Perovskite Materials for Solar Cell Applications: Electronic Structure, Optical Transitions, and Directional Charge Transport, *J. Phys. Chem. C*, 2016, **120**, 29039–29046.
75 K. K. Bass, L. Estergreen, C. N. Savory, J. Buckeridge, D. O. Scanlon, P. I. Djurovich, S. E. Bradforth, M. E. Thompson and B. C. Melot, Vibronic Structure in Room Temperature Photoluminescence of the Halide Perovskite Cs_3 Bi_2 Br_9, *Inorg. Chem.*, 2017, **56**, 42–45.
76 G. Xiang, Y. Wu, M. Zhang, J. Leng, C. Cheng and H. Ma, Strain-induced enhancement of carrier transport and optical absorption in $Cs_3Bi_2Br_9$ perovskite, *Solid State Commun.*, 2022, **354**, 114918.
77 B. Liu, X. Feng, M. Long, M.-Q. Cai and J. Yang, Designing Surface-Functionalized Ti3C2T2-Cs3Bi2Br9 (T = O, Cl, OH, or F) Heterostructures for Perovskite Optoelectronic Applications, *Phys. Rev. Appl.*, 2022, **18**, 054036.
78 H. Zhang, Y. Xu, Q. Sun, J. Dong, Y. Lu, B. Zhang and W. Jie, Lead free halide perovskite $Cs_3Bi_2I_9$ bulk crystals grown by a

low temperature solution method, *CrystEngComm*, 2018, **20**, 4935–4941.

79 C. Liu, Y. Wang, H. Geng, T. Zhu, E. Ertekin, D. Gosztola, S. Yang, J. Huang, B. Yang, K. Han, S. E. Canton, Q. Kong, K. Zheng and X. Zhang, Asynchronous Photoexcited Electronic and Structural Relaxation in Lead-Free Perovskites, *J. Am. Chem. Soc.*, 2019, **141**, 13074–13080.

80 H. Wu, W. Liu, W. Ma, T. Liang, X. Liu and J. Fan, Special roles of two-dimensional octahedral frameworks in photodynamics of Cs3Bi2Br9 nanoplatelets: Electron and lattice-wave localization, *Appl. Phys. Lett.*, 2022, **121**, 181902.

81 F. Iannone, F. Ambrosino, G. Bracco, M. De Rosa, A. Funel, G. Guarnieri, S. Migliori, F. Palombi, G. Ponti, G. Santomauro and P. Procacci, *2019 International Conference on High Performance Computing & Simulation (HPCS)*, IEEE, Dublin, Ireland, 2019.

82 A. Mariano, G. D'Amato, F. Ambrosino, G. Aprea, F. Buonocore, M. Celino, A. Colavincenzo, M. Fina, A. Funel, S. Giusepponi, G. Guarnieri, F. Palombi, S. Pierattini, G. Ponti, G. Santomauro, G. Bracco and S. Migliori, Fast Access to Remote Objects 2.0 a renewed gateway to ENEAGRID distributed computing resources, *Future Gener. Comput. Syst.*, 2019, **94**, 920–928.